# NUMERICAL ANALYSIS OF FREE-TO-ROLL WING ROCK MOTION BY THE FLUID DYNAMICS-FLIGHT DYNAMICS COUPLING

**Masataka Hirano *, Koji Miyaji ****
*** Grad. School of Yokohama National University, 79-5 Tokiwadai, Hodogaya-ku, Yokohama, 240-8501 Japan.**
**E-mail:** hirano@yal.asl.seg.ynu.ac.jp
**** Yokohama National University, 79-5 Tokiwadai, Hodogaya-ku, Yokohama, 240-8501 Japan.**
**E-mail:** miyaji-k@ynu.ac.jp

**Keywords**: *Delta wing, Unsteady aerodynamics, Computational Fluid Dynamics*

## Abstract

*A wing rock is known to be a self-excited rolling oscillation of a delta wing that is induced by unsteady aerodynamic forces. In this study, free-to-roll simulations are carried out by incorporating time-accurate computational fluid dynamics with an equation of motion of a wing. A limit cycle oscillation and the histogram of a hysteresis in the rolling moment, which has four peaks within one cycle, are successfully simulated. The strength of the leading-edge vortices at a fixed roll angle is rather different from that during the wing rock especially at large angular velocities and it causes the characteristic behavior of the unsteady moments.*

## 1 Introduction

Delta wings require high angles of attack at landing or taking-off due to its low lift inclination although they are quite suitable for high-speed cruise conditions at transonic or supersonic flight. One of the serious problems of delta wings encountered at high angles of attack is a “wing rock.” It is known to be a self-excited rolling oscillation that is induced by unsteady aerodynamic forces. The investigation and the prediction of the phenomenon are important to improve the stability and the performance of a delta wing at landing or taking-off. If a dynamic characteristic can be predicted, more advanced designs are possible for future high-speed airplanes.

A number of studies have been carried out on the wing rock by both experiments and numerical simulations [1-4]. In the experiments, the measured value is mainly a time history of the roll angle and it is difficult to measure unsteady aerodynamic forces or to visualize unsteady flow fields. In this study, a time-accurate numerical simulation is carried out to clarify the wing rock phenomenon. A computational fluid dynamics (CFD) is incorporated with the dynamics of a wing and the equations are solved simultaneously. The unsteady aerodynamic forces and the motion of the leading-edge separation vortices of a delta wing are carefully examined by the comparison between the unsteady simulations and the static simulations with fixed roll angles.

## 2 Flow conditions

A low-speed wind tunnel experiment [1] is numerically simulated. The motion of a delta wing has one degree-of-freedom around the root-chord axis, namely, the motion is free to roll. The leading-edge sweepback angle is 82.5 degrees, the wing thickness is 0.67 % based on the chord length. The angle of attack is 28.5 degrees, which is constant in the wing rock motion, and Reynolds number is $4.2 \times 10^5$ based on the chord length. Freestream Mach number is

set to 0.2 to simulate the low-speed flow in the experiment. The moment of inertia of the delta wing around the rolling axis, $I_x$, is 191 [g•cm$^2$]. The time history of the roll angle $\phi$ obtained by the experiment [1] is shown in Fig. 1.

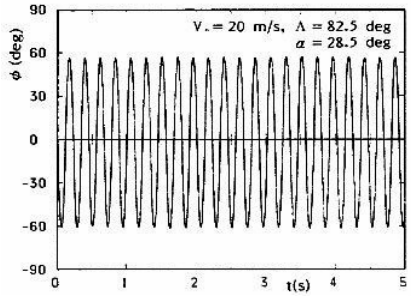


Fig. 1. Time history of the roll angle in the experiment[1]

## 3 Numerical Algorithms

The governing equations for the fluids are the 3D thin-layer Navier-Stokes equations. They are solved by the finite difference method. Numerical fluxes for the inviscid terms are the Roe's flux difference splitting and spatially 3rd-order accuracy is attained by the MUSCL interpolation. Viscous terms are discretized by the 2nd-order central difference. The LU-ADI implicit time integration method [5] is used. The original LU-ADI is developed for steady state computations and it has less than 1st-order accuracy in time. It is modified to have 2nd-order accuracy for the current objectives. The following 3-point backward differencing implicit equation is solved by the Newton iteration and the LU-ADI method,

$$\frac{3}{2\Delta t}Q^{n+1}-\frac{2}{\Delta t}Q^{n}+\frac{1}{2\Delta t}Q^{n-1}=-R\left(Q^{n+1}\right) \quad (1)$$

where $Q$ is conservative variables of the fluid equations and $R$ is the residual, or, the steady terms in the Navier-Stokes equations.

The grid movement in the fluid calculation is reflected by considering the wall boundary condition and the time-derivative terms of the metrics as shown in the following.

$$u=x_\tau, v=y_\tau, w=z_\tau \quad (2)$$

$$\begin{aligned}\xi_t &= \left(\xi_x x_\tau+\xi_y y_\tau+\xi_z z_\tau\right)\\ \eta_t &= \left(\eta_x x_\tau+\eta_y y_\tau+\eta_z z_\tau\right)\\ \zeta_t &= \left(\zeta_x x_\tau+\zeta_y y_\tau+\zeta_z z_\tau\right)\end{aligned} \quad (3)$$

As for the dynamics of the delta wing, the following equation of motion is considered to simulate the free-to-roll wind tunnel experiment,

$$I_x\frac{d^2\phi}{dt^2}=M_r \quad (4)$$

where $M_r$ is the rolling moment due to the aerodynamic forces. The above equation is solved by the 2-step Runge-Kutta method. Given the $M_r$ from $Q$ in Eq. (1), the roll angle $\phi$ at the next time step is obtained by solving the Eq. (4). Then the grid movement is specified and the new flow variables, $Q$, are obtained from Eq. (1).

Figure 2 shows the computational grid around the delta wing. It consists of 71 points in the chord direction, 131 points in the circumferential direction and 65 points in the radial direction, in total 604,565 points.

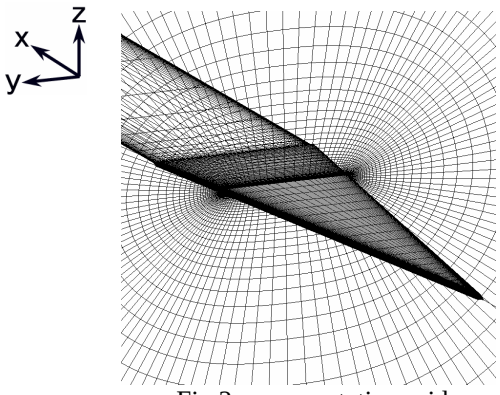


Fig.2. computation grid

## 4 Results and discussion

### 4.1 Result of forced-rolling simulation

As a preliminary computation, one of the authors carried out the flow simulation around a delta wing in forced oscillation [6]. The time-history shown in Fig. 1 is approximated by the sinusoidal curve. The amplitude and the

frequency normalized by the freestream velocity and the span length are set to match the experimental result. Numerical Algorithms and the computational grid are same, except that the original LU-ADI time integration method is used.

Figure 3 shows the roll angle versus rolling-moment coefficient plot. The result of a forced oscillation shows the hysteresis in the plot as was observed in the experiment. However, the kinetic energy of the wing received from the unsteady flow (closed area at the center of the plots) apparently exceeds the energy lost against the flow (closed area at both ends of the plots), and then, the results qualitatively contradicts the experimental results. The result shows the necessity of the free-to-roll simulation. The energy balance within one cycle of the oscillation is discussed in detail in the following sections.

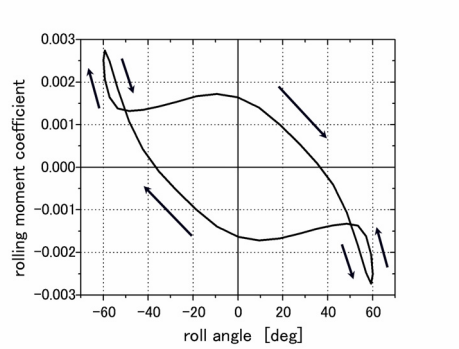


Fig. 3. Rolling-moment coefficient v.s. roll angle (forced-rolling simulation [6]

## 4.2 Wing motion by free-to-roll simulations

Figure 4 shows the time history of the roll angle by the free-to-roll simulation. In Fig. 4, the original LU-ADI and the 2nd-order LU-ADI with Newton iterations are compared. The solid line is the calculation result with the 2nd-order time accuracy and the dotted line is the result of the original LU-ADI method. Both simulation results reproduce the transitions from the initial steady state at 28.5 degrees-A.O.A to the limit cycle oscillation. The amplitude of the roll angle and the reduced frequencies for the experiment [1] are $\phi_{\max} = 60$ [deg] and $\Omega = 0.05$, respectively. Those of the original LU-ADI simulation are $\phi_{\max} = 43.4$ [deg], $\Omega = 0.064$, and those of the 2nd-order LU-ADI with Newton iterations are $\phi_{\max} = 48.5$ [deg], $\Omega = 0.060$, respectively. The quantitative differences between the two schemes are small but other features are rather different as discussed below.

Figures 5 and 6 show the time histories of the roll angular acceleration by the experiment [1] and the present study. The simulations capture characteristic behavior of the angular acceleration, namely, there exist four peaks within one cycle, although the second peaks after the maximum/minimum values are not so clear in the simulations.

Figures 7 and 8 show the angular acceleration versus the roll angle. The time-accurate simulation well predicts the trend in the experiment. The hysteresis in the plots is the cause of the limit cycle oscillations. The delta wing receives energy from the air flow when the sign of the moment is the same as that of the roll-angular velocity while it loses energy when their signs are different in figure 7, 8. As a result, the area enclosed by the upper and lower curves containing the origin stands for the energy received from the flow, and the closed area at both ends of the plot stands for the energy lost. The energy gain and loss balance within one cycle oscillation. In the experiment, Fig. 7, the second peaks of the rolling moment after the maximum/minimum values appear near the roll angles at which the curves intersect and the feature is well reproduced by the time-accurate simulation in Fig. 8. In addition, almost linear change of the roll-angular acceleration with respect to the roll angle just after the second peaks agrees between the experiment and the time-accurate simulation. Hereafter, only the result by the time-accurate simulation is discussed.

Figure 9 again shows the roll angle vs. the rolling moment with the solid line indicating the motion with the positive roll-angular velocity, $\dot{\phi} > 0$, and the dotted line indicating the negative roll-angular velocity, $\dot{\phi} < 0$. The steady-state flow computations with fixed roll angles are also shown by the dashed-lines with

square symbols. The static rolling moment distribution shows nonlinear behavior at $|\phi|$ >10°, and the rolling moment reaches maximum /minimum at $|\phi|$ =20°. In the free-to-roll oscillation, both the minimum magnitude of the rolling moment (state B) and the angles are larger than those of the static computation. The rolling moment at the maximum roll angle in the unsteady simulation (state C) is the same as the steady simulation since $\dot{\phi} = 0$ at the state C. When the roll angle $\phi$ decreases from the state C to the second peak (state E) in the rolling moment, the change in the rolling moment is rather small but the roll-angular velocity $\dot{\phi}$ is rapidly varies as shown in Fig. 10.

The rolling moments in Fig. 9 are divided into Figs. 11 and 12, which show the rolling moments acting on the upper and the lower surfaces, respectively. In Fig. 11, the kinetic energy of the wing received from the flow is apparently positive, while in Fig. 12, the lower surface loses energy against the flow except the small region where $|\phi| > 20^{\circ}$. In Fig. 11, not only a qualitative behavior of the hysteresis, but also the roll angles at which the first and the second peaks of the rolling moment appear are almost the same as the overall moments in Fig. 9. Thus, the wing rock motion is governed by the aerodynamic forces on the upper surface of the wing.

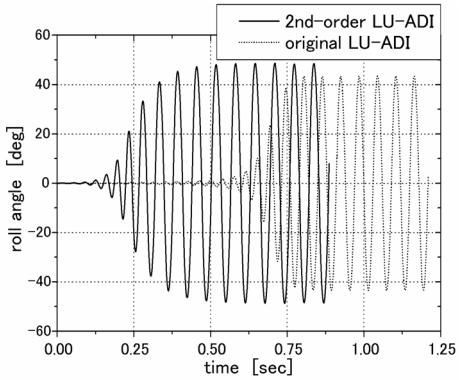


Fig. 4. Time history of the roll angle (comp. )

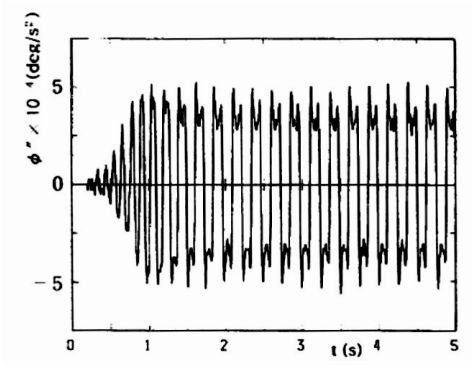


Fig. 5. Time history of the roll-angular acceleration (exp.[1])

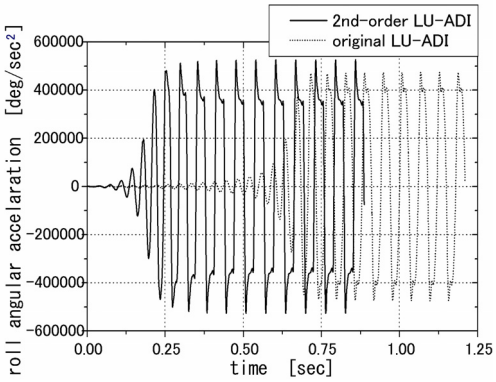


Fig. 6. Time history of the roll-angular acceleration (comp.)

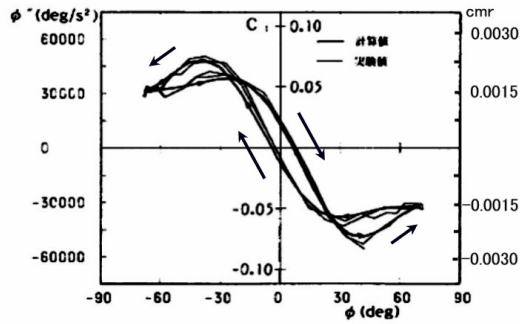


Fig. 7. Roll angular acceleration and rolling moment coefficient v.s. roll angle (exp[1])

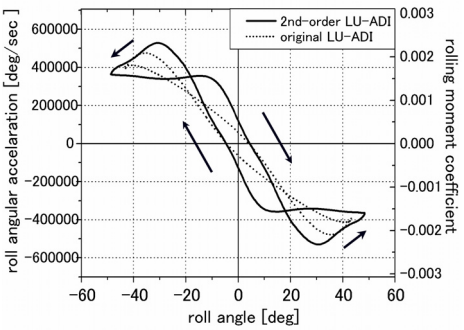


Fig. 8. Roll angular acceleration and rolling moment coefficient v.s. roll angle (comp.)

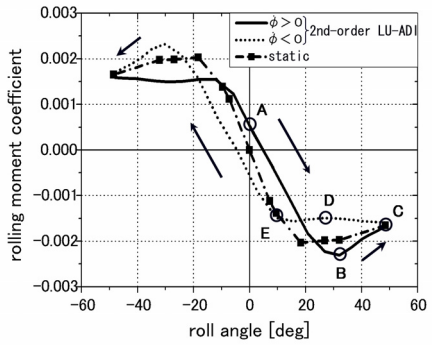


Fig. 9. Rolling moment coefficient v.s. roll angle

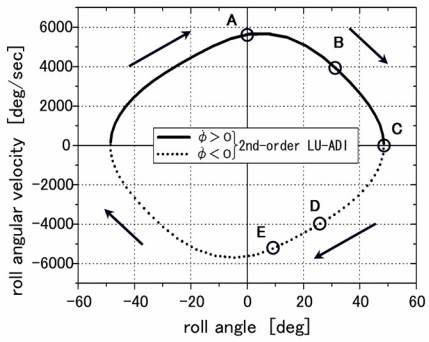


Fig. 10. Roll angular velocity v.s. roll angle

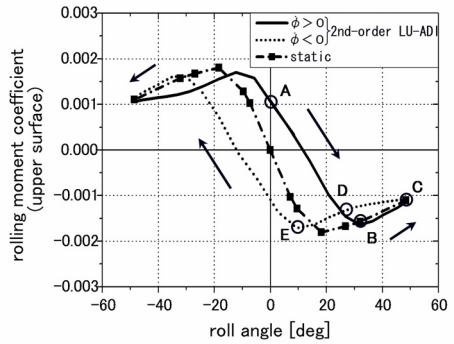


Fig. 11. Rolling moment coefficient at upper surface v.s. roll angle

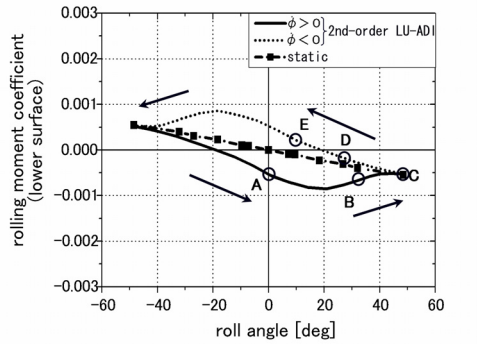


Fig. 12. Rolling moment coefficient at upper surface v.s. roll angle

## 4.3 Flow-field analysis

The characteristic behavior of the rolling moment is further investigated by analyzing the flow field. Figure 13 shows the locations of the vortex core within one cycle and figures 14(a) – 18(a) are the comparison of the total pressure contour plots between the instantaneous solution during the wing rock motion and the steady-sate solution at the same, fixed roll angles. Figures 14(b) – 18(b) are the surface pressure distributions at 64 % chord section. Figures 14 – 18 respectively correspond to the state A - E in Fig. 9 - 13. The roll angular velocity and the rolling moment are defined positive in counter-clockwise direction.

A) $\phi = 0.0[\text{deg}],\ \dot{\phi} > 0$ (Fig.14.)

If the wing doesn't rotate, the leading-edge vortices become symmetric as shown in the right-hand side of Fig. 14(a). In the wing rock motion shown in the left-hand side of Fig. 14(a), the separation vortex at y<0 is vertically extended while the vortex at y>0 is pressed onto the upper surface of the wing since the roll-angular velocity is positive, $\dot{\phi} > 0$. As a result, the negative pressure gets larger and a positive rolling moment is generated.

B) $\phi = 32.1[\text{deg}],\ \dot{\phi} > 0$ (Fig.15.)

The rolling moment at the state B reaches the minimum value within the cycle. The roll-angular velocity still has a small positive value, and then the negative pressure peak due to the primary and the secondary vortex is lower than the steady computation with a fixed roll angle. The pressure distribution at y>0 shows the wing motion works to increase the rolling moment both on the upper and the lower surfaces. That is why the absolute values of the maximum or the minimum rolling moment in the wing rock

motion are larger than those of the steady computation.

C) $\phi = 48.5\,[\mathrm{deg}],\ \dot{\phi} = 0$ (Fig.16.)

The roll angle reaches the maximum and $\dot{\phi} = 0$ at the state C. Both the rolling moment and the pressure distribution are almost equal to the steady computation. The vortex is laterally extended and the core moves to the center of the wing as shown in Fig. 13, then the magnitude of the rolling moment becomes smaller than that at the state B.

D) $\phi = 26.9\,[\mathrm{deg}],\ \dot{\phi} < 0$ (Fig.17.)

After the state C ( $\dot{\phi} = 0$ ), the magnitude of the roll angular velocity rapidly increases. The change of the rolling moment is small around the state D because the traverse of the vortex from the center to the leading edge (solid line in Fig.13) causes the decrease in the rolling moment acting on the upper surface (Fig. 11) while the compression on the lower surface causes the increase in the rolling moment (Fig. 12).

E) $\phi = 9.6\,[\mathrm{deg}],\ \dot{\phi} < 0$ (Fig.18.)

The rolling moment reaches the second peak at the state E. The traverse of the vortex in the lateral direction becomes small while the vortex is pressed to the wing surface due to the motion, then the pressure on the upper surface at y<0 decreases. The vortex at y>0 cannot follow the wing motion, and the peak of the negative pressure is hardly seen. Therefore, the moment in the clockwise direction on the upper surface is larger than that of the static computation. But the pressure on the lower surface works to suppress the increase in the magnitude of the moment, then the second peak of the overall moment becomes smaller than the first peak.

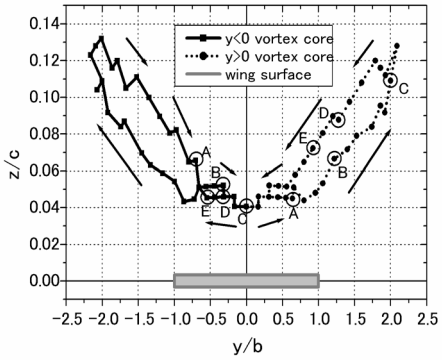


Fig. 13. Location of the vortex core at 64 % chord section (looking-from-behind)

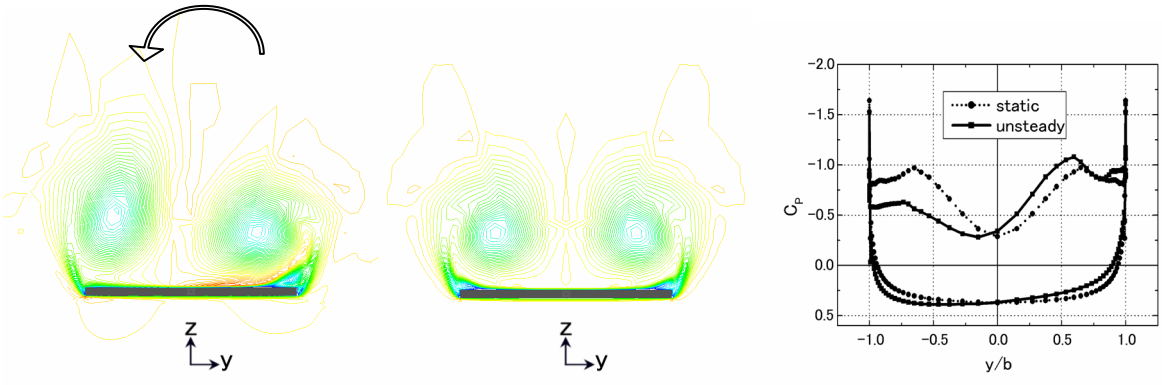


unsteady static

(a) total pressure contour line (b) pressure coefficient

Fig. 14. $\phi = 0.0\,[\mathrm{deg}],\ \dot{\phi} > 0$ (looking-from-behind, counter-clockwise in roll axis is positive) state A

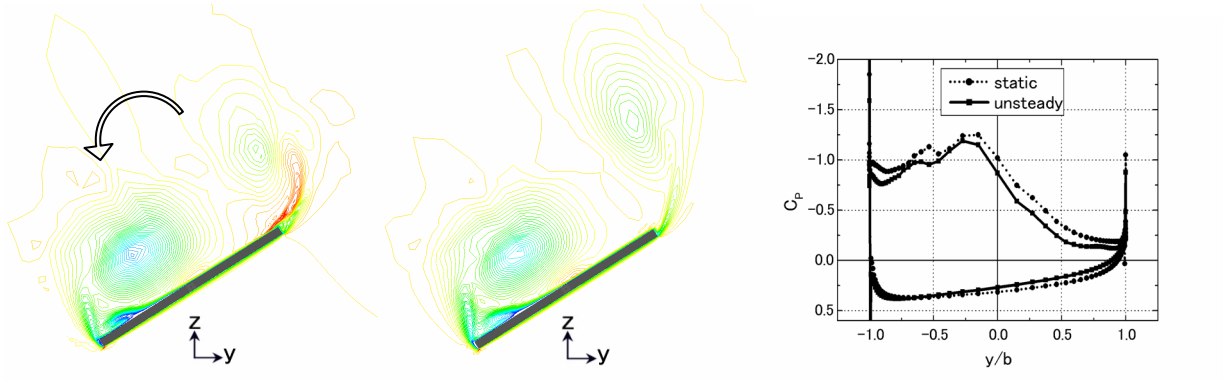


unsteady static

(a) total pressure contour line (b) pressure coefficient

Fig. 15. $\phi = 32.1[\text{deg}]$, $\dot{\phi} > 0$ (looking-from-behind, counter-clockwise in roll axis is positive) state B

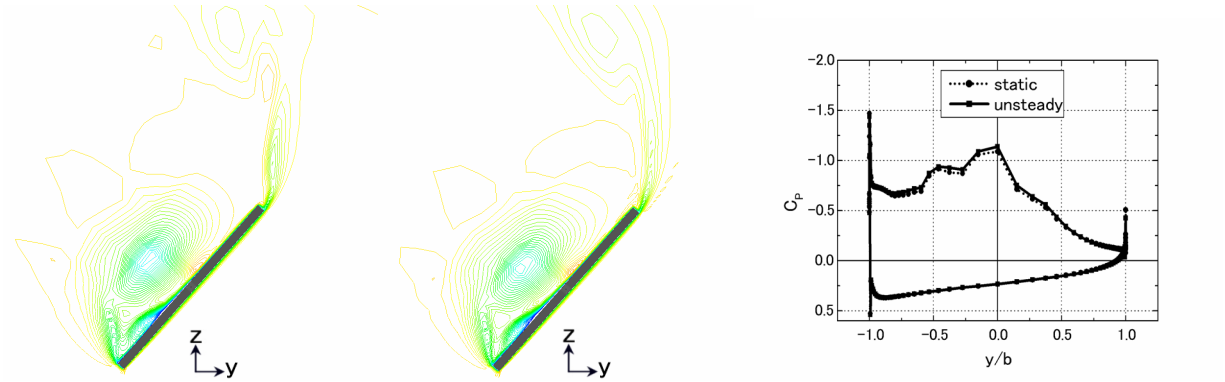


unsteady static

(a) total pressure contour line (b) pressure coefficient

Fig. 16. $\phi = 48.5[\text{deg}]$, $\dot{\phi} = 0$ (looking-from-behind, counter-clockwise in roll axis is positive) state C

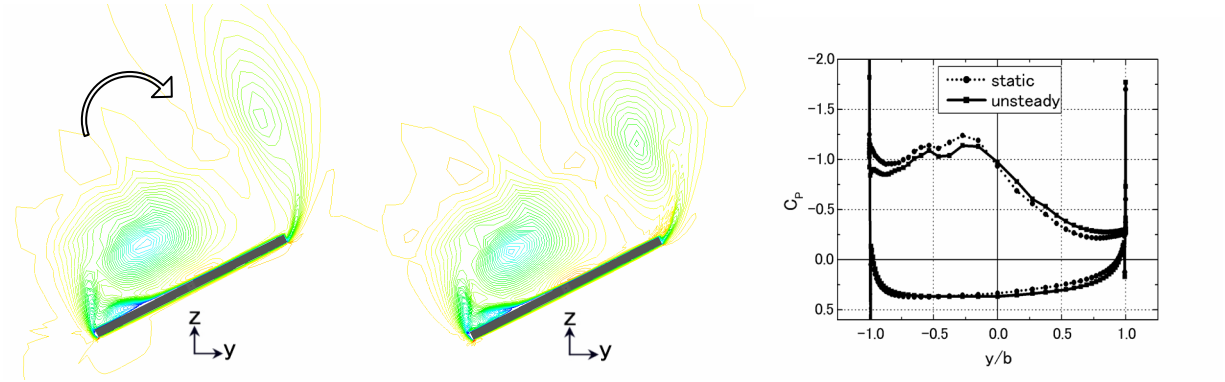


unsteady static

(a) total pressure contour line (b) pressure coefficient

Fig. 17. $\phi = 26.9[\text{deg}]$, $\dot{\phi} < 0$ (looking-from-behind, counter-clockwise in roll axis is positive) state D

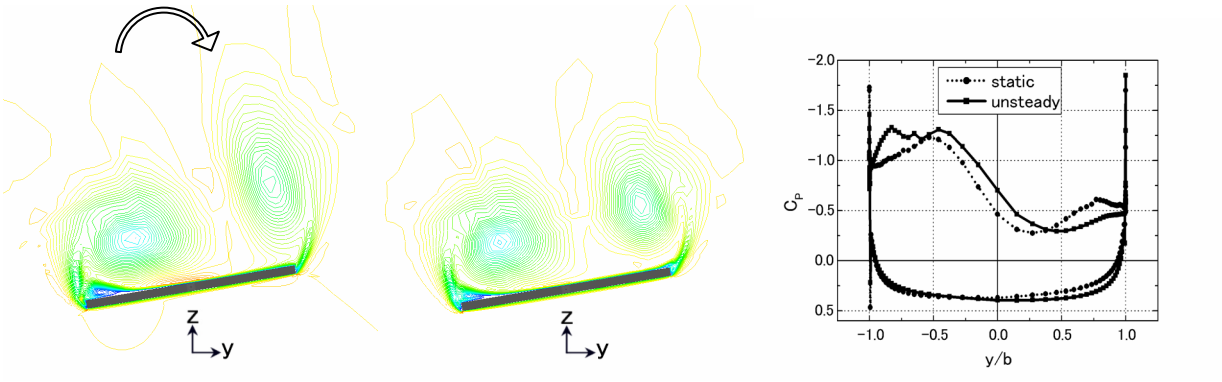


unsteady static

(a) total pressure contour line (b) pressure coefficient

Fig. 18. $\phi = 9.6[\mathrm{deg}]$, $\dot{\phi} < 0$ (looking-from-behind, counter-clockwise in roll axis is positive) state E


Table. 1. Comparison result between the simulation and the experiment

| | Roll angle amplitude [deg] | Period [sec] | Dimensionless frequency | Maximum roll angular acceleration [deg/sec$^2$] | Maximum rolling moment coefficient |
|---|---|---|---|---|---|
| Experiment [1] | 60.0 | 0.225 | 0.05 | $4.80\times10^{4}$ | $2.55\times10^{-3}$ |
| Original LU -ADI | 43.4 | 0.061 | 0.064 | $4.74\times10^{5}$ | $2.09\times10^{-3}$ |
| 2nd-order LU-ADI | 48.5 | 0.064 | 0.060 | $5.26\times10^{5}$ | $2.32\times10^{-3}$ |

### 4.4 Quantitative comparison of the experiment and the simulation result

Important quantities describing the oscillation are compared between the experiment and the simulations. The amplitude of the roll angle, the period, the dimensionless frequency, the maximum roll angular acceleration and the maximum rolling moment coefficient are shown in Table 1. The dimensionless frequency and the maximum rolling moment coefficient show good agreement between the experiment and the time-accurate simulation. The reason for the disagreement for the dimensional values, namely, the amplitude, period and roll angular acceleration, are possibly due to the difference in the freestream velocity between the experiment and the simulations. Essentially incompressible fluid simulation should be conducted.

## 5. Summary

A self-induced oscillation around the roll axis of a delta wing, wing rock, is well simulated. The characteristic profile of the angular acceleration (rolling moment) of the wing rock is also reproduced. They are investigated by relating the movement of the leading-edge separation vortices with the motion of the wing. The time accuracy is important for the correct simulation and the evaluation of the dimensionless frequency and the rolling moment. The improvement of the space accuracy or the simulation at the same freestream velocity as the experiment is necessary to enhance the accuracy and reliability.

## References

[1] Tate A, Noda J and Yoshinaga T. Wing Rock of Delta Wings with an Analysis by Phase Plane Method, *NAL TR-1266*, 1995. (in Japanese)

[2] Hsu C. H. and Lan C. E. Theory of Wing Rock, *Journal of Aircraft*, No.22, pp.920-924, 1985.

[3] Kwak D. Y. Experimental Study of Roll Dynamic of Delta Wings with Force-to-Roll Oscillation, *Jornal of the JSASS*, No.48, pp.495-500, 2000.

[4] Chaderjian N. M. and Schiff L. B. Numerical Simulation of Forced and Free-to-Roll Delta-Wing Motions, *Journal of Aircraft*, No.33, pp.93-99, 1996. (in Japanese)

[5] Obayashi S, Matsushima K, Fujii K and Kuwahara K. Improvement in Efficiency and Reliability for Navier-Stokes Computations Using the LU-ADI Factorization Algorithms, *AIAA* Paper 86-338, 1986.

[6] Koji K, Maeda S. Numerical Simulation of Unsteady Aerodynamic Forces Acting on a Delta Wing in Rolling Oscillations, *The 30th Visualization Symposium*, pp.439-442, 2002. (in Japanese)